Research Article

ADVANCED
PHOTONICS
NEXUS

Manipulable multipurpose nanothermometers based on a fluorescent hybrid glass fiber microsphere cavity

Dandan Yang,[a] **Jianhao Chen**,[a] **Jiachang Wu**,[a] **Hao Zhang**,[a] **Xiaofeng Liu**,[b] **Jianrong Qiu**,[c] **Zhongmin Yang**,[d] and **Guoping Dong**[a,*]

[a]South China University of Technology, School of Materials Science and Engineering, State Key Laboratory of Luminescent Materials and Devices, Guangzhou, China
[b]Zhejiang University, School of Materials Science and Engineering, Hangzhou, China
[c]Zhejiang University, College of Optical Science and Engineering, State Key Laboratory of Modern Optical Instrumentation, Hangzhou, China
[d]South China University of Technology, School of Physics and Optoelectronics, Guangzhou, China

Abstract. Fluorescent nanothermometers for remote temperature measurement at the micro/nanoscale have stimulated growing efforts in developing efficient temperature-responsive materials and detection procedures. However, the efficient collection and transmission of optical signals have been a tremendous challenge for practical applications of these nanothermometers. Herein, we design an all-fiberized thermometry based on a fiber-coupled microsphere cavity coated with thermo-sensitive $NaYF_4{:}20\%Yb^{3+},2\%Er^{3+}@NaYF_4$ nanocrystals (NCs), allowing for spatial temperature sensing with resolution down to the few-micrometer scale. In our design, the microsphere efficiently excites the NCs and collects their upconversion emissions, and the use of a fiber splitter coupled with the microsphere allows for lossless routing of excitation and emitted light. We demonstrate the use of this all-fiber temperature sensor in diverse environments, especially in strongly acidic and alkaline conditions. Leveraging the high flexibility of commercial silica fiber, this all-fiber temperature sensor was employed for stable fixed-point real-time temperature measurement and multipurpose temperature recording/mapping in opaque environments, microscale areas, various solutions, and complicated bent structures. Thus, the demonstrated design could have strong implications for the practical use of nanothermometers in various possible scenarios, especially monitoring temperatures in diverse physiological settings.

Keywords: nanothermometers; fluorescence thermometry; multipurpose temperature detection; temperature imaging; fiber microsphere cavity.

Received Apr. 7, 2024; revised manuscript received May 4, 2024; accepted for publication May 22, 2024; published online Jun. 13, 2024.

[DOI: 10.1117/1.APN.3.4.046004]

1 Introduction

Fluorescent nanomaterials possessing thermal-responsive fluorescence properties [Fig. 1(a)] can be used for remote and high-sensitivity thermal readouts at the micro/nanoscale.[1] Such nanomaterials have been extensively exploited as nanothermometers, and numerous researchers continue to work on their design and synthesis.[2–4] In recent years, advanced physicochemical synthetic routes have led to the discovery of attractive temperature-sensitive properties in a wide range of different fluorescent nanomaterials, including deoxyribonucleic acid (DNA) or protein-conjugated systems, small organic compounds, dye-doped polymeric nanoparticles, lanthanide-ion-doped nanoparticles, and quantum dots.[5–9] These nanothermometers with high spatial resolution (<10 μm), short acquisition time (<1 ms), capability of remote operation, and high relative thermal sensitivity have found numerous potential applications in nanofluidics, catalytic reactions, microelectronics, and perhaps most importantly, cell

---

*Address all correspondence to Guoping Dong, dgp@scut.edu.cn

biology, preclinical research, and diagnostics.[10–14] Despite the fact that the recently developed nanothermometers are radically more sophisticated, encompassing complex synthetic procedures, they always face a fundamental problem: practical temperature detection is often hampered by difficulties in optical signal collection and transmission. For example, optical thermometry based on fluorescence prevents most such nanothermometers from temperature measurement in opaque environments. The extreme spatiotemporal resolution is only accessible with state-of-the-art real-time superresolution imaging techniques, which, however, is not suitable for most practical applications. Furthermore, the difficulty in locating and immobilizing fluorescent nanoparticles makes their use for accurate-position temperature measurement almost impossible. Thus, these pressing issues inspire us to construct a platform for fluorescent nanothermometers to realize manipulable real-time temperature sensing and further operate in a variety of complicated environments.

Recently, whispering gallery mode (WGM) optical microresonators have attracted intense interest. The unique combination of high-quality (Q) factors and small mode volumes in a WGM resonator significantly enhances the light field and leads to an extraordinarily high light intensity inside the resonator with a modest input power, which is due to a strong interaction between the light field and the objects placed in the cavity mode volume.[15] Among the WGM resonators, microsphere cavities confine the light through total internal reflection [Fig. 1(b)], and both transverse electric and transverse magnetic propagating modes keep high Q factors.[16,17] Coating Tm^{3+}-doped nanoparticles onto the microsphere cavity, upconverted lasing with an ultralow threshold of continuous-wave excitation was achieved at room temperature.[18,19] This result suggests that the microsphere cavity could be an efficient method to collect the fluorescence signals by coating the nanothermometers onto its surface [Fig. 1(c)]. Encouragingly, at the glass softening temperature, glass fibers could be used to fabricate high-quality microsphere cavities driven by surface tension.[20,21] Separately, optical fibers exhibit the advantages of light weight, small size, large bandwidth, high signal light transmission efficiency, and freedom from electromagnetic interference.[22–25] These unique advantages make glass fibers a feasible and effective choice to transmit the fluorescence signals collected by the microsphere cavities.

Here, we demonstrate the development of an all-fiber temperature sensor based on a fiber-coupled microsphere cavity coated with rare earth (RE)-doped upconversion (UC) nanocrystals (NCs). With the use of a fiber splitter, both the excitation and emission lights are efficiently coupled in and out of the fiber

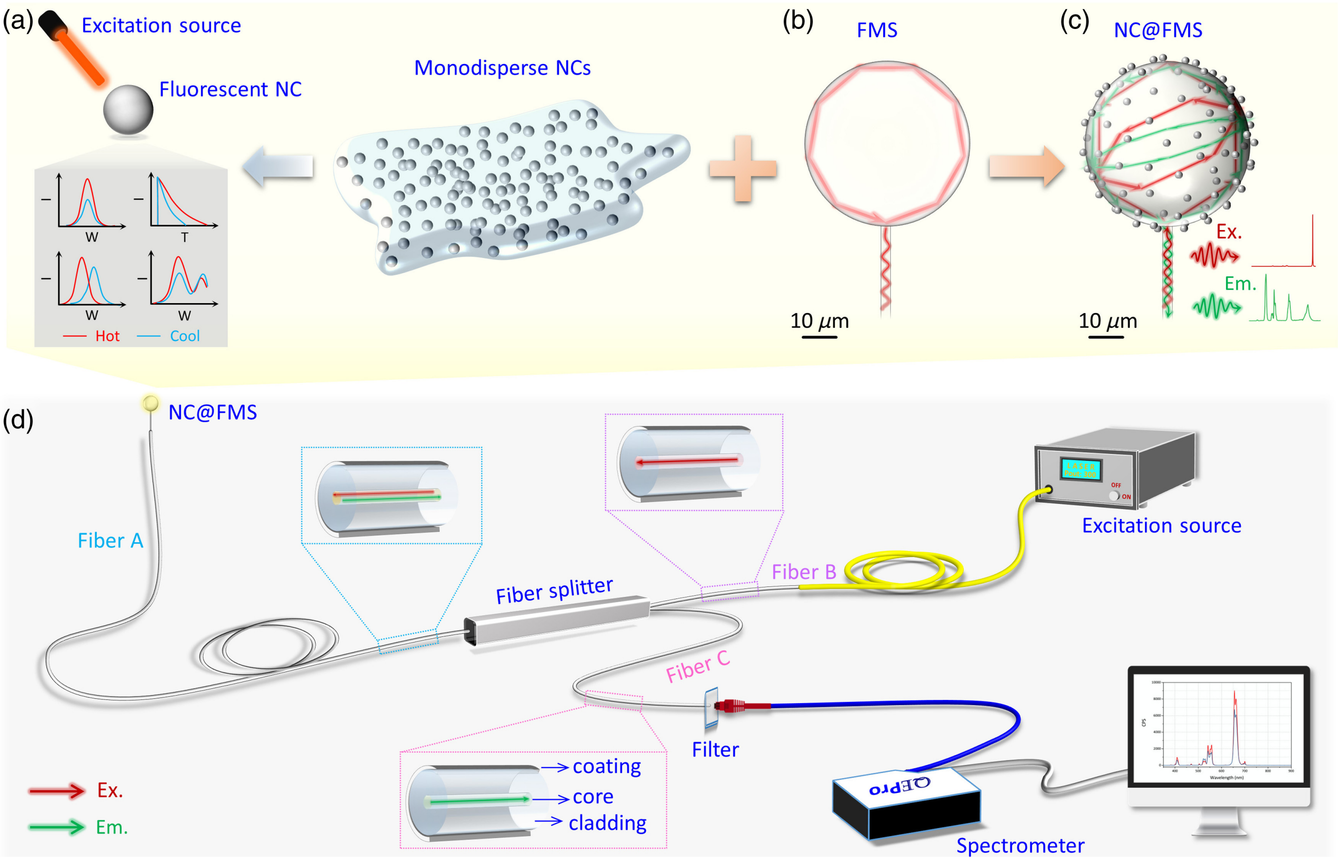

Fig. 1 Schematic representation of the NC@FMS all-fiber temperature sensor. (a)–(c) Schematic design of temperature sensing using the NC@FMS: (a) temperature-sensing strategies of nanomaterials relying on emission intensity, lifetime, peak position, and fluorescence intensity ratio (FIR); (b) schematic of total internal reflection of light in an FMS; (c) schematic of excitation and emission in an NC@FMS. (d) Schematic design of all-fiber temperature sensing based on the NC@FMS. The insets in panel (d) illustrate the purpose of different fiber segments.

microsphere (FMS), as shown in Fig. 1. Benefiting from the thermometric response of the UC emission from the NCs, the designed NC-coated FMS (NC@FMS) all-fiber temperature sensor shows high accuracy over a wide temperature window. With excellent stability, micrometer-level spatial resolution, and high flexibility, the NC@FMS all-fiber temperature sensors can be used for remote temperature monitoring and real-time, high-precision temperature recording in opaque environments, trace solutions, microscale areas, complex bent structures, and multidimensional temperature fields. These successful temperature measurements demonstrate that our fiber-coupled hybrid microsphere cavity design greatly promotes the real applications of nanothermometers in demanding scenarios. More importantly, the designed all-fiber nanothermometer could be promising for monitoring temperature in a human body almost regardless of tissue penetration depth of the emissions.

2 Results and Discussion

2.1 Fabrication and Properties of the Designed NC@FMS All-Fiber Temperature Sensor

Our design concept based on the fiber-coupled microsphere cavity has been implemented following the unique total reflection of light in microsphere cavities and optical fibers. Silica fiber as a single-component fiber has a wide softening temperature range, favorable mechanical properties after softening, and high transmittance in a wide spectral region.[26,27] Thus, silica fibers can be fabricated into high-quality microspheres that allow for simultaneous transmission of the excitation and emission lights from most fluorescence NCs by total reflection. The realization of low-threshold lasers through coating various light emitters onto a silica microsphere[28–30] illustrates that most fluorescent NCs can be efficiently excited in this well-designed all-fiber platform. The commercialization of silica fiber enables us to introduce a fiber splitter fabricated with the same commercial silica fiber to fuse with the tail fiber of the FMS for realizing all-fiberization. Moreover, the low cost of commercial silica fibers is another essential factor that encourages us to choose them for the fabrication of the FMS and the all-fiber paths. The recent development of the fluorescence intensity ratio (FIR) thermometric technique from RE ions has inspired the design of upconverting RE-based nanothermometers for many applications, particularly in hyperthermia and photothermal therapeutic approaches.[3] Meanwhile, an $NaYF_4$ host with a refractive index comparable to that of silica glass[31] can ensure the leaking of more excitation light reflected in the FMS into the outer surface layer of NCs and the coupling of more emission light from the surface NCs into the FMS, thereby improving the signal readout accuracy. Accordingly, a widely studied Yb^{3+}-Er^{3+} co-doped $NaYF_4$ NC with a high UC efficiency is considered as the ideal nanothermometer in our design.

To obtain morphology- and size-uniform NCs for homogeneous coating and enhanced fluorescence intensity for accurate signal reading, we prepared a multilayer core-shell nanostructure consisting of $NaYF_4:20\%Yb^{3+},2\%Er^{3+}@NaYF_4$ using a modified multistep co-precipitation method.[32] The as-synthesized core-shell NCs with a hexagonal structure exhibit a monodisperse spherical morphology with an average size of 45 nm [Fig. 2(a); Figs. S1 and S2(a) in the Supplementary Material]. Under 980 nm excitation, typical visible UC emissions of Er^{3+} were detected, and the outer $NaYF_4$ layer eliminates possible surface quenching effects, resulting in a much enhanced UC intensity [Fig. S3(a) in the Supplementary Material]. Following a method similar to fiber splicing,[33] we fabricated FMSs with different diameters driven by the surface tension. A CO_2 laser beam is employed to heat and soften a silica fiber tip, which then transforms into a sphere of controllable size. The scanning electron microscopy (SEM) image in Fig. 2(b) confirms the smooth surface of the obtained FMS that benefits a high Q factor and a strong light local field. The surface oleate ligands introduced during the synthetic process [Fig. S2(b) in the Supplementary Material] endow the as-synthesized NCs with outstanding hydrophobicity. Such hydrophobic NCs can be deposited onto the surface of microspheres by partial swelling of microspheres in a polar solvent mixture to drive van der Waals interactions between the hydrophobic surface of NCs and the outer region of the microspheres.[18] Thus, we immersed the fabricated FMSs into a cyclohexane dispersion of the as-synthesized NCs to coat the NCs onto the FMSs [see Fig. S4(a) in the Supplementary Material]. The SEM image of an NC@FMS in Fig. 2(c) definitely presents the successfully deposited NCs on the FMS surface through this solution-phase process. Observations in Figs. S4(b)–S4(f) in the Supplementary Material suggest that a high NC concentration is beneficial to acquire homogeneous coating.

Subsequently, we fused the tail fiber of a homogeneous coated FMS to a fiber splitter to construct an all-fiber sensing platform, as shown in Fig. S5 in the Supplementary Material. With the all-fiber optical paths, we successfully detected the visible UC emissions from the surface $NaYF_4:20\%Yb^{3+},2\%Er^{3+}@NaYF_4$ NCs [Fig. 2(d)]. In the microscopic dark field, obviously, the surface NCs are sufficiently excited [inset in Fig. 2(d)] and the FMS effectively localizes the emissions and couples them into fiber paths [Fig. S3(b) in the Supplementary Material]. The ultra-low transmission loss of the commercial silica fiber allows the designed NC@FMS all-fiber sensor to perform remote temperature measurement by adjusting the length of fiber optical paths [Fig. 2(e)]. While the good stability of both NCs and silica fibers enables the designed NC@FMS all-fiber sensors to be stable in diverse environments (e.g., organic solution, water, and strong alkali), importantly, after drying in the air again, the emission intensities can be completely restored [Figs. 2(f)–2(h); Figs. S6(a) and S7(a)–S7(c) in the Supplementary Material]. The SEM images in Figs. S8(a)–S8(c) in the Supplementary Material show that after immersion in these environments for 20 min, the FMSs are still coated with many NCs, consistent with the above spectroscopic results. The different intensity changes in different environments [Figs. 2(f)–2(h)] arise from the different refractive index differences between the FMS and the environments. However, by immersing the NC@FMS in a strong acid, its emission intensities immediately decrease and cannot be restored after drying in the air (Figs. S6(b) and S7(d) in the Supplementary Material], as there are only a few NCs left on the FMS surface [Fig. S8(d) in the Supplementary Material], which is because acid could release the oleate ligands from the NC surface through protonation.[34] This confirms that the stable coating of as-synthesized NCs onto the FMS results from the van der Waals interaction between the organic ligands of NCs and the outer region of the microsphere. It is worth noting here that the extremely weak blue emissions at ∼410 and 470 nm that are assigned to the $^2H_{9/2} \rightarrow {}^4I_{15/2}$ and $^2K_{15/2} \rightarrow {}^4I_{13/2}$ transitions of Er^{3+} (Refs. 35 and 36) were also detected from the NC@FMS [see the enlarged spectrum in Fig. 2(d)]. This is owing to the effective coupling of the UC

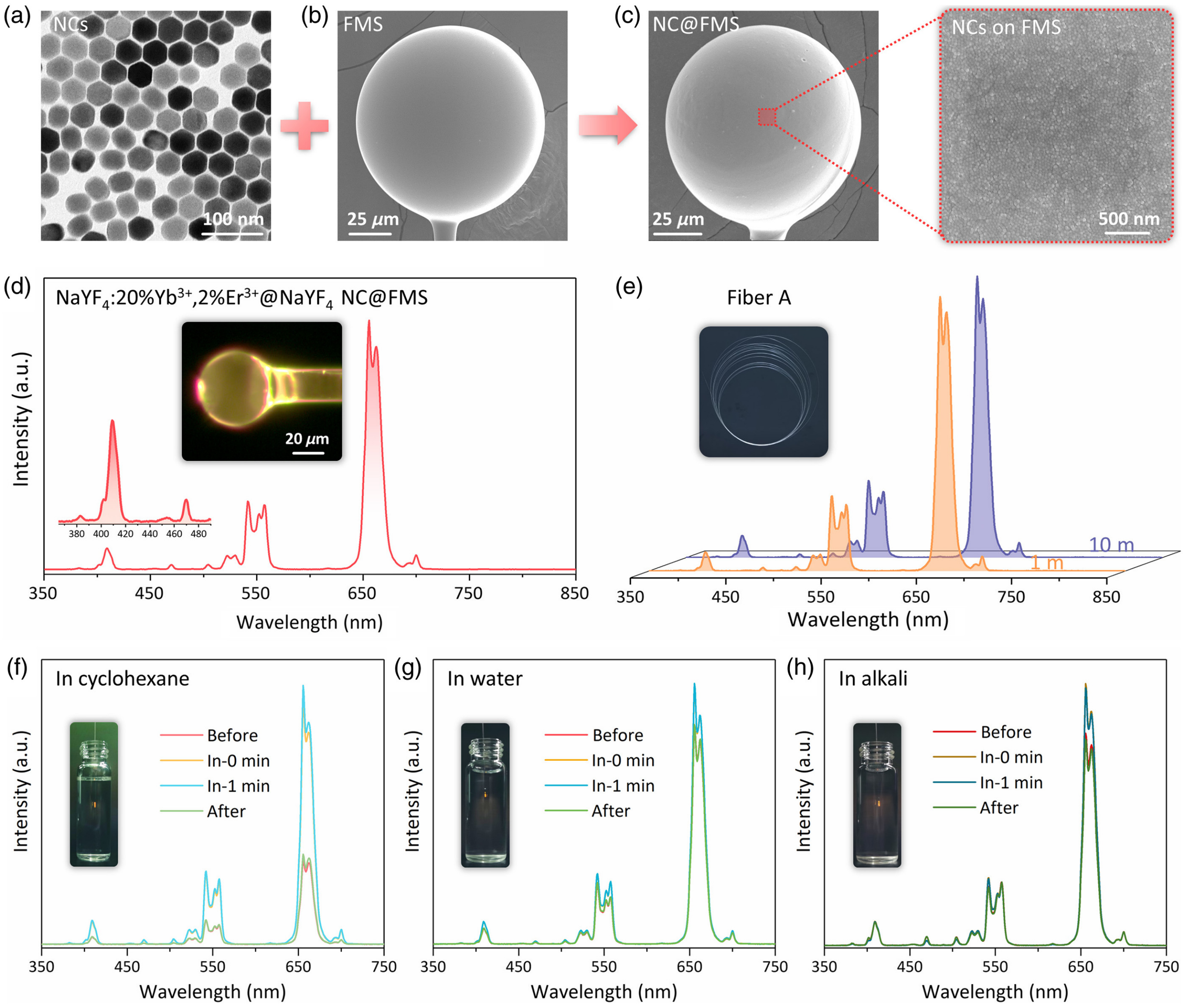

Fig. 2 Properties of the designed NC@FMS all-fiber temperature sensor. (a) Transmission electron microscope (TEM) image of the as-synthesized $NaYF_4:20\%Yb^{3+},2\%Er^{3+}@NaYF_4$ NCs. (b) SEM image of a silica FMS. (c) SEM images of the $NaYF_4:20\%Yb^{3+},2\%Er^{3+}@NaYF_4$ NC@FMS and its surface structures. (d) Photoluminescence (PL) spectrum of the $NaYF_4:20\%Yb^{3+},2\%Er^{3+}@NaYF_4$ NC@FMS all-fiber sensor under 980 nm fiber laser excitation. The insets are the corresponding microscopic fluorescent photograph and the enlarged spectrum from 365 to 490 nm. (e) PL spectra of the $NaYF_4:20\%Yb^{3+},2\%Er^{3+}@NaYF_4$ NC@FMS all-fiber sensor with different fiber A [as labeled in Fig. 1(d)] lengths under 980 nm fiber laser excitation. The inset is the photograph of fiber A. (f)–(h) PL spectra of the $NaYF_4:20\%Yb^{3+},2\%Er^{3+}@NaYF_4$ NC@FMS all-fiber sensor before, during, and after immersion in different environments for 1 min: (f) in cyclohexane, (g) in water, and (h) in alkali. The insets are the fluorescent photographs of the NC@FMS in different environments.

emissions within the microsphere cavity modes, indicating that our design also could utilize weak fluorescence emissions for temperature sensing.

2.2 Thermometric Performance of the Designed NC@FMS All-Fiber Temperature Sensor

In the as-synthesized NCs, Yb^{3+} ions with a much larger absorption cross section at 980 nm strongly absorb the incident 980 nm photons[37] and then sensitize Er^{3+} ions, realizing stronger UC emissions (Fig. S9 in the Supplementary Material). Specially, the $^2H_{11/2} \rightarrow {}^4I_{15/2}$ ($I_H = 522$ nm) and $^4S_{3/2} \rightarrow {}^4I_{15/2}$ ($I_S = 542$ nm) transitions are in close proximity in energy that leads to a thermal equilibrium governed by the Boltzmann law.[4] Therefore, based on the strongly temperature-dependent green emissions of Er^{3+}, we placed an NC@FMS with an FMS diameter of ~50 μm onto a metal heater to perform temperature calibration of the corresponding all-fiber sensor (Fig. S10 in the Supplementary Material). The two green emissions change synchronously with the temperature [Fig. 3(a)],

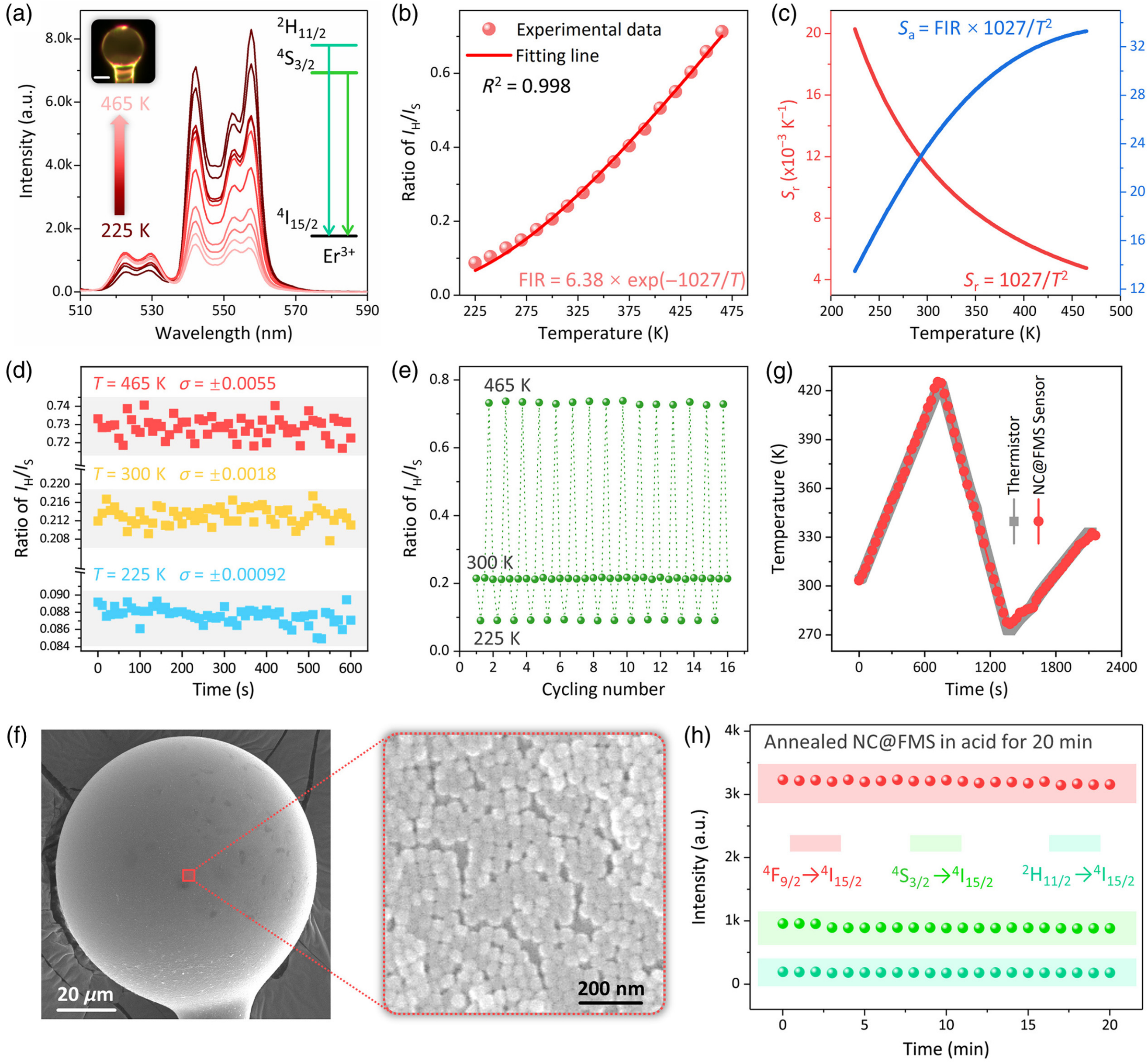

Fig. 3 Thermometric performance of the $NaYF_4:20\%Yb^{3+},2\%Er^{3+}@NaYF_4$ NC@FMS all-fiber temperature sensor. (a) Green fluorescence response of the all-fiber sensor to temperature ranging from 225 to 465 K. The inset on the left is the microscopic fluorescent photograph of the NC@FMS at room temperature. Scale bar: 15 μm. The inset on the right shows the energy levels from which emissions are observed. (b) Experimental data and fitted curve of FIR (${}^2H_{11/2}/{}^4S_{3/2}$) against the absolute temperature. (c) Absolute and relative sensitivities of the all-fiber temperature sensor. (d) FIR (${}^2H_{11/2}/{}^4S_{3/2}$) fluctuations of the all-fiber temperature sensor over time at the constant temperatures of 225, 300, and 465 K. (e) Temperature cycling test of the all-fiber temperature sensor between 225 and 465 K. (f) SEM images of the NC@FMS and its surface structures after the thermometric testing. (g) Comparison of the temperature response between the commercial thermistor and the all-fiber temperature sensor. (h) Emission intensity fluctuations of the annealed NC@FMS all-fiber temperature sensor over time when in an acidic environment.

and an exponential relation exists between FIR values and absolute temperature (T) in the temperature range from 225 to 465 K [Fig. 3(b)], which consists of the Boltzmann law, as expected from Eq. (4) (as detailed in Sec. 4.6). Hence, one can easily measure or monitor the temperature using the $NaYF_4:20\%Yb^{3+},2\%Er^{3+}@NaYF_4$ NC@FMS all-fiber temperature sensor. Figure 3(c) provides the absolute sensitivity [S_a, obtained through Eq. (5) in Sec. 4.6] and relative sensitivity [S_r, obtained through Eq. (6) in Sec. 4.6] values. The S_r is comparable to those of previously reported Er^{3+}-doped nanomaterials (Table S1 in the Supplementary Material), indicating that the FMS and fiber paths only collect and transmit the emitted

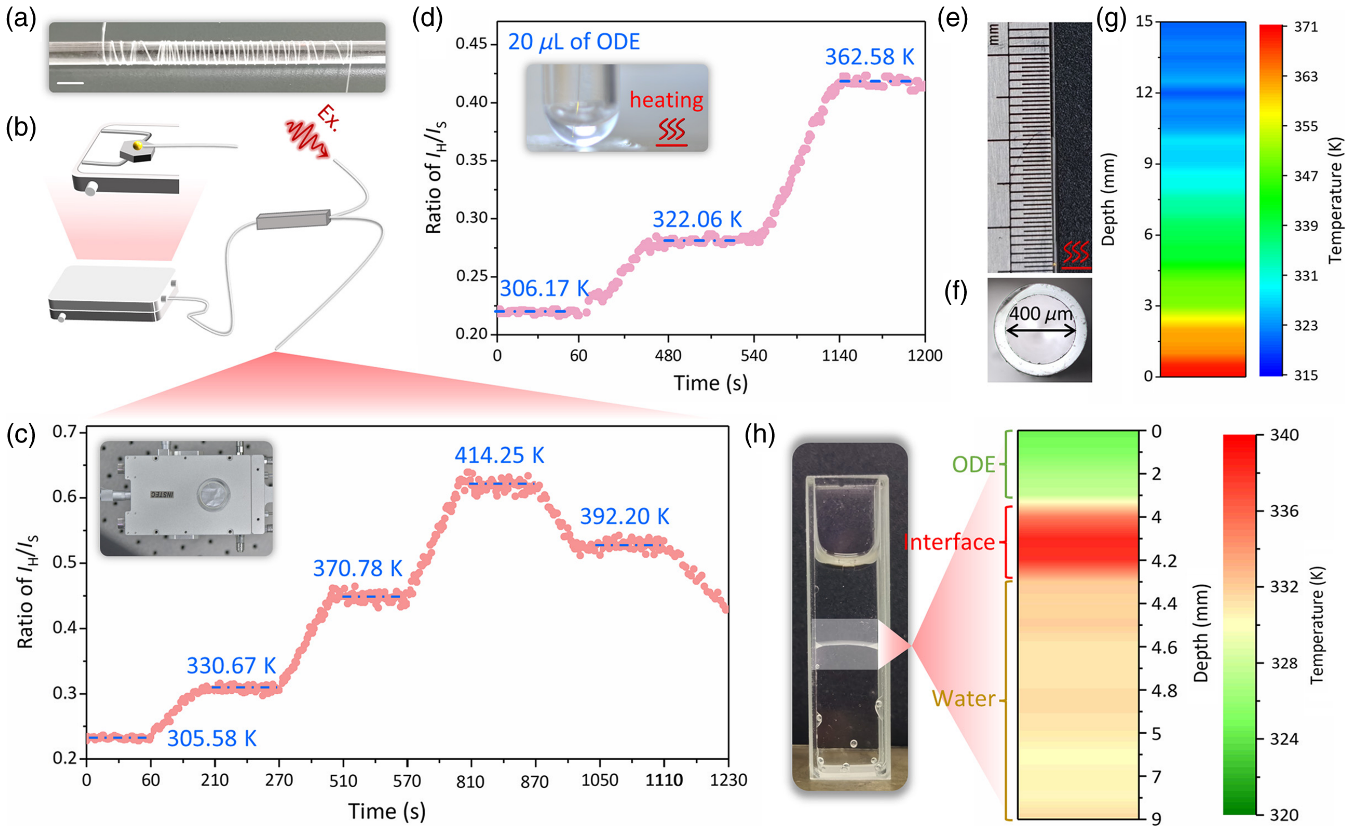

Fig. 4 Applications of the $NaYF_4:20\%Yb^{3+},2\%Er^{3+}@NaYF_4$ NC@FMS all-fiber temperature sensors in enclosed spaces and microscale areas. (a) Photograph of the commercial silica fiber wrapping around a glass rod. Scale bar: 5 mm. (b) Schematic of the NC@FMS all-fiber temperature sensor performing fixed-point temperature detection in an enclosed space. (c) Temperature changes with time in an enclosed space monitored using the NC@FMS all-fiber temperature sensor. The inset shows the corresponding photograph. (d) Temperature changes with time in 20 μL of heated 1-octadecene (ODE) monitored using the NC@FMS all-fiber temperature sensor. The inset is the photograph of the NC@FMS when in the heated ODE. (e) Photograph of the NC@FMS all-fiber temperature sensor inserted in a capillary tube. (f) End face photograph of the capillary tube in panel (e). (g) Interior temperature distribution of the capillary tube in the thermal field measured using the NC@FMS all-fiber temperature sensor. (h) Interfacial temperature distribution between water and ODE measured using the NC@FMS all-fiber temperature sensor.

photons and have no effect on the thermometric performance of the coated NCs. With increasing measurement time, the detected FIR values (I_{522}/I_{542}) and green intensities at 522 and 542 nm fluctuate in a very small range at the constant temperatures of 225, 300, and 465 K [Fig. 3(d); Figs. S11(a) and S11(b) in the Supplementary Material], suggesting that the all-fiber temperature sensor is quite stable. After 15 response cycles in the temperature range of 240 K and two continuous temperature change tests, the sensor maintains good reproducibility and shows stable and repeatable temperature detection [Fig. 3(e); Figs. S11(c), S11(d), and S12 in the Supplementary Material]. The NCs on the FMS surface do not fall off obviously after one cycle of the thermometric performance testing [Fig. 3(f)], which contributes to the high reproducibility. In addition, we tested the temperature response between the all-fiber sensor on the metal heater and the thermistor placed in a suit. The demodulation results in Fig. 3(g) show that the sensor could mostly synchronize the changes with the thermistor, demonstrating that the all-fiber temperature sensor can respond accurately and quickly to temperature changes.

We also coated the $NaYF_4:20\%Yb^{3+},2\%Er^{3+}$ core NCs onto the surface of an FMS with a diameter of ~50 μm and tested the temperature sensing of the corresponding all-fiber sensor. Its good thermometric performance (Fig. S13 in the Supplementary Material) indicates that our designed all-fiber platform can be used as a general system for fluorescent nanothermometers. Furthermore, by adjusting the fabrication parameters of the FMS, FMSs of different sizes are fabricated, and the resultant NC@FMS all-fiber temperature sensors demonstrate a tunable spatial resolution (Fig. S14 in the Supplementary Material). In Fig. S14(a) in the Supplementary Material, we controlled the FMS size below 10 μm, illustrating that the spatial resolution of our designed all-fiber temperature sensor can reach a few-micrometer scale. However, the $NaYF_4:20\%Yb^{3+},2\%Er^{3+}@NaYF_4$ NC@FMS presents poor intensity stability at a higher temperature and no longer follows the Boltzmann law at a lower temperature (Fig. S15 in the Supplementary Material), which may be due to the decomposition of organic ligands and formation of defects.[38] Thermal treatment is a convenient and effective way to eliminate the organic ligands and structure defects in nanomaterials prepared by chemical synthetic methods.[39] Thus, we annealed the $NaYF_4:20\%Yb^{3+},2\%Er^{3+}@NaYF_4$ NC@FMS at 250°C for 3 h and then connected it to a fiber splitter. Although melting and agglomeration occur for the coated NCs [Fig. S16(a) in the Supplementary Material], the NCs preserve the hexagonal structure and provide thermal-sensitive green emissions in a wider temperature range as compared with the pristine NCs [Figs. S16(b) and S16(c) in the Supplementary Material]. In the temperature range from 195 to 510 K, the curve of I_{522}/I_{542} versus T shows good exponential fitting, and the FIR values exhibit small fluctuation when increasing measurement time and good reproducibility in 15 cycles [Fig. S16(d)–S16(f) in the Supplementary Material]. In addition, the annealed NC@FMS all-fiber temperature sensor has almost the same temperature response as the commercial thermistor [Fig. S16(g) in the Supplementary Material]. Consequently, thermal treatment to as-synthesized NCs improves the thermometric performance of the all-fiber sensor, suggesting that the optimization of nanothermometers alone can improve the thermometric performance of the designed all-fiber sensing platform. Intriguingly, the slight melting during the annealing process makes the NCs attach strongly to the FMS surface; therefore, the annealed NC@FMS all-fiber temperature sensor exhibits high stability for measurement in a strongly acidic environment [Fig. S17(a) in the Supplementary Material]. Even after immersion for 20 min, the fluorescence performance and surface of the annealed NC@FMS do not show any evident structural change [Fig. 3(h); Fig. S17(b) in the Supplementary Material]. After comparing the thermometric performance of the illustrative NC@FMS all-fiber temperature sensors (Table S2 in the Supplementary Material), there is no significant difference in their calculated energy gap (ΔE), S_a and S_r. This further reveals that the fiber-coupled microsphere has no effect on the thermometric performance of the coated nanothermometers but can efficiently collect and transmit the detection signal.

2.3 Applications of the Designed NC@FMS All-Fiber Temperature Sensor

Commercial silica fiber is highly flexible, as displayed in Fig. 4(a), which shows that it easily wraps around a glass rod with a diameter of 5 mm. Leveraging the good stability and high spatial resolution down to the micrometer scale, it is possible to manipulate the NC@FMS for temperature measurement in some special scenarios. First, we put the NC@FMS in an enclosed and opaque space to monitor the temperature at a particular location [Fig. 4(b)]. The sensor responds quickly and stably at a large temperature range [Fig. 4(c); Fig. S18 in the Supplementary Material]. So, the all-fiber platform realizes nanothermometers for precise real-time temperature monitoring in some special dark environments, such as electromagnetic interference environments. Second, the NC@FMS has stable fluorescence output, leading to stable fixed-point temperature monitoring in trace solutions, as exemplified here by 20 μL of water or 1-octadecene (ODE) [Fig. 4(d); Figs. S19 and S20 in the Supplementary Material]. In addition, by manipulating the fiber path, the NC@FMS can move in the trace solutions and accurately monitor its temperatures at different depths (Fig. S21 in the Supplementary Material). By increasing the control precision of the fiber path, the temperature distribution in a microscale area can be mapped. Figures 4(e)–4(g) show the temperature distribution mapping in a heated capillary tube with an internal diameter of 400 μm, which is obtained by inserting the NC@FMS in it, and the temperature is measured at intervals of 500 μm (Fig. S22 in the Supplementary Material). These results could have strong implications for precise temperature measurement in microfluidics and catalytic reactions.

The high-precision temperature point acquisition allows the NC@FMS all-fiber temperature sensor to be used in certain scenarios that are not easily amenable to existing thermometric strategies. By stepwise moving the NC@FMS at a high resolution, we mapped the temperature distribution at the interface of a heated mixed liquid using this all-fiber sensor with an FMS diameter of 50 μm [Fig. 4(h)]. The interface has a higher temperature, and its dimension is less than 500 μm [Figs. S23(a)–S23(c) in the Supplementary Material], which cannot be easily obtained by existing commercial thermometers. It should be noted here that although different environments would cause a change in the fluorescence intensity at 522 and 542 nm for the NC@FMS, the FIR value is not affected, as the relative change in intensity at the two wavelengths is almost the same [Figs. S23(d) and S23(e) in the Supplementary Material]. Furthermore, we employed the NC@FMS to measure the photoluminescence (PL) spectra at 1 mm intervals in a three-dimensional (3D) temperature field with a dimension of 5 mm × 5 mm × 5 mm [Fig. S24(a) in the Supplementary Material]. According to the detected PL spectra, we successfully drew a 3D temperature mapping. As shown in Fig. 5(a), we can clearly observe the temperature distribution in 3D space, which breaks through the dimensional limit of the infrared thermal imaging technique. In addition, using the designed all-fiber temperature sensor, we obtained the complete thermal information of a temperature field with any size, including the exact temperature at arbitrary points [Fig. S24(b) in the Supplementary Material], the temperature distribution [Fig. 5(a)], and the temperature gradient [Fig. S24(c) in the Supplementary Material].

Intriguingly, in Fig. 5(b), the fluorescent NC@FMS moves freely in an S-type capillary tube by manipulating the fiber path, such that the interior temperature at different positions can be measured according to the corresponding PL spectra [Fig. S25(a) in the Supplementary Material]. When the S-type capillary tube is positioned in temperature fields, the interior temperature distribution can be mapped by moving the NC@FMS with 2 mm intervals [Figs. 5(c) and 5(d); Figs. S25(b) and S25(c) in the Supplementary Material]. Moreover, the NC@FMS can move freely and perform accurate temperature measurements in a U-shaped tube with a larger curvature and size (Fig. S26 in the Supplementary Material). These results reveal that the NC@FMS all-fiber temperature sensor with high flexibility can be used in various complex bent structures, especially in blood vessels. As shown in Figs. S27(a) and S27(b) in the Supplementary Material, fiber transmission allows the temperature measurement using this sensor in opaque artificial blood, and monitoring its temperature changes with time. For this demonstration, we fill artificial blood into an artificial blood vessel with an inner diameter of 900 μm to simulate human blood vessels. The NC@FMS moves inside this vessel easily and accurately measures temperature at arbitrary positions [Fig. 5(e)]. Thus, this all-fiber platform enables the measurement of temperature in a human body without consideration of the tissue penetration depth of the emissions from nanothermometers. Furthermore, other fluorescent nanothermometers with better

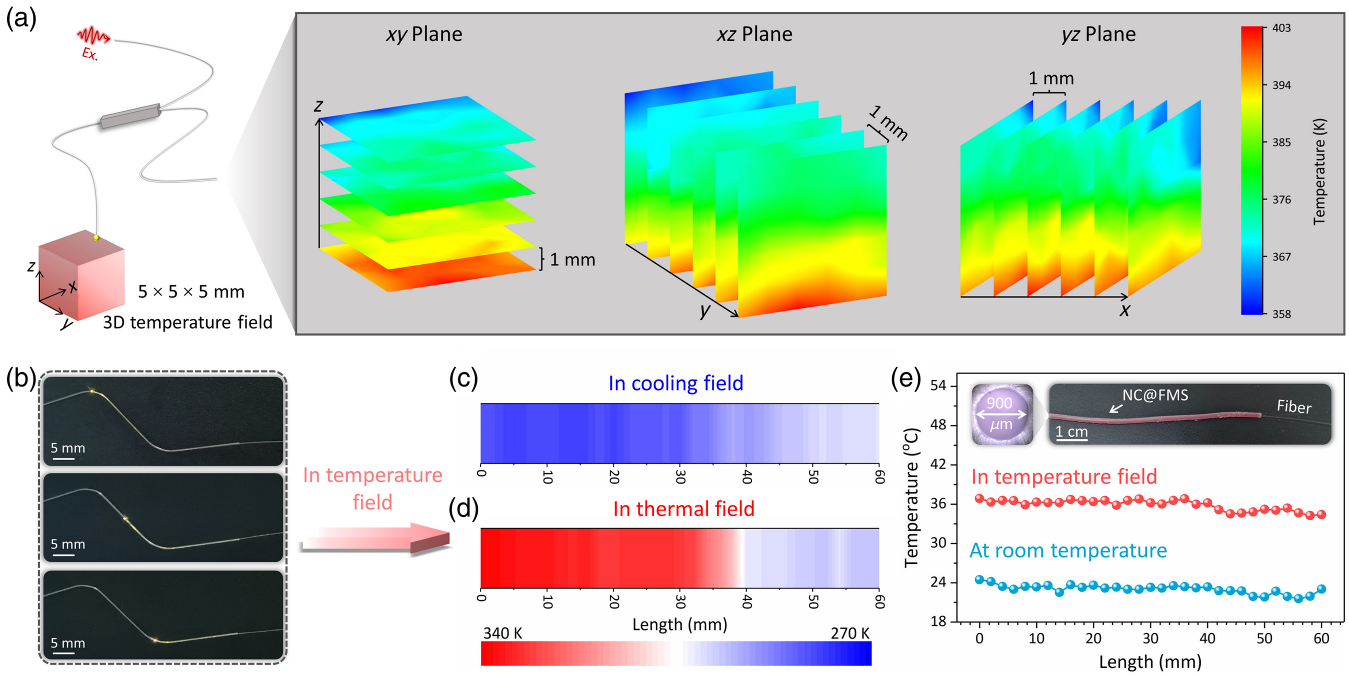

Fig. 5 Applications of the $NaYF_4:20\%Yb^{3+},2\%Er^{3+}@NaYF_4$ NC@FMS all-fiber temperature sensors in complicated structures. (a) Temperature distributions of different planes in the micro-area 3D temperature field with a dimension of 5 mm × 5 mm × 5 mm by measuring the temperature at 1 mm intervals using the NC@FMS all-fiber temperature sensor. (b) Photographs of the NC@FMS all-fiber temperature sensor measuring the interior temperature of an S-type capillary tube. (c) and (d) Interior temperature distributions of the S-type capillary tube when in (c) a cooling field or (d) a thermal field measured using the NC@FMS all-fiber temperature sensor. (e) Temperatures at different positions of the artificial blood vessel measured using the NC@FMS all-fiber temperature sensor. The insets show the photograph of the all-fiber sensor inserted in the artificial blood vessel and its inner diameter. The temperature at the location of the heating source in the temperature field is 38°C.

thermometric performance but with emissions outside of the biological window can be used based on this design, which could be promising for cell biology, preclinical research, and diagnostic applications. As provided in Figs. S27(c) and S27(d) in the Supplementary Material, the S_a and S_r values of the NC@FMS all-fiber temperature sensor within a small temperature range (33°C to 45°C) were calculated to be $0.0028°C^{-1}$ and $1.164\%°C^{-1}$, which are comparable with those of previously reported electrical sensors.[40]

3 Conclusion

In summary, by uniformly coating monodisperse upconverted NCs onto a fiber-coupled FMS cavity with minimized scattering loss, we have shown that the UC emissions from NCs can be efficiently collected and transmitted through the FMS and fiber paths, respectively. Thereby, an NC@FMS all-fiber temperature sensor with high stability, repeatability, and accuracy based on the thermally coupled levels (TCLs) of Er^{3+} ($^2H_{11/2}$ and $^4S_{3/2}$) has been constructed. We verified that this all-fiber temperature sensor has good stability, which enables its stable fluorescence output in various environments, such as water, organic solutions, and even strong alkalis. Moreover, by adjusting the size of the FMS, the all-fiber temperature sensor demonstrates tunable spatial resolution from less than 10 μm to more than 100 μm. The performance can be improved by the thermal treatment of coated NCs, such that the annealed all-fiber sensor can be used for temperature measurement in a wider temperature range and harsh liquid environments with good stability and accuracy. By the combination of high spatial resolution and flexibility, the all-fiber temperature sensor allows for stable real-time temperature measurements in closed-dark spaces, trace solutions, microscale areas, and complex ben structures. In addition, the high-precision fixed-point temperature recording enables multidimensional temperature mapping, from which temperatures at arbitrary locations, temperature gradient, and temperature distribution can be precisely determined. This all-fiber optic design demonstrated here provides an easy and convenient strategy for the development of fluorescent nanosensors with efficient collection and transmission of optical signals and significantly leverages the advantages of nanothermometers for temperature measurement in complicated and demanding scenarios, especially for monitoring human body temperature and constructing completed thermal information of multidimensional temperature fields.

4 Appendix: Experimental Section

4.1 Materials

The starting materials were oleic acid (OA, 90%), ODE (90%), $RE(CH_3CO_2)_3$ (99.9%) (RE = Y, Yb, and Er), NaOH (≥98%),

NH_4F (≥98%), and methanol (reagent grade). All of these materials were purchased from Sigma–Aldrich (St. Louis, Missouri, United States) and used as received unless otherwise noted. The solution of $RE(CH_3CO_2)_3$ (0.2 M) was prepared by dissolving RE salt in distilled water within an ultrasonic bath. The methanol solution of NH_4F (0.4 M) was prepared by dissolving the appropriate amount of NH_4F in methanol within an ultrasonic bath.

4.2 Synthesis of $NaYF_4:20\%Yb^{3+},2\%Er^{3+}$ Core NCs

The $NaYF_4:20\%Yb^{3+},2\%Er^{3+}$ core NCs were synthesized through a multistep co-precipitation method, as previously reported, with some modifications.[32] In a typical synthesis, 3 mL of OA and 7 mL of ODE were added into a 50-mL round bottom flask, followed by the addition of 2 mL of $RE(CH_3CO_2)_3$ (0.2 M) (Y:Yb:Er = 78:20:1, mol%) stock solution. The mixed solution was heated to 150°C under stirring for 1 h to form a lanthanide-oleate and then cooled to room temperature. Then, 1 mmol of NaOH was dissolved into 1 mL of methanol with ultrasonic agitation. At room temperature, the NaOH-methanol stock solution was pipetted into 4 mL of NH_4F-methanol (0.4 M) stock solution. After vortexing for 10 s, the mixture was quickly injected into the reaction flask. Subsequently, the mixture was heated to 50°C, kept at this temperature for 0.5 h, and then heated to 100°C for 1 h under vacuum to remove methanol. Then, the mixture was heated to 290°C and incubated at 290°C for 1.5 h under an argon atmosphere. After the reaction, the flask was cooled to room temperature, and the precipitation NCs were collected by centrifugation at 8000 r/min for 5 min. The obtained NCs were washed several times with ethanol and cyclohexane and finally dispersed in 4 mL of cyclohexane for subsequent use.

4.3 Synthesis of $NaYF_4:20\%Yb^{3+},2\%Er^{3+}@NaYF_4$ Core-Shell NCs

The $NaYF_4:20\%Yb^{3+},2\%Er^{3+}@NaYF_4$ core-shell NCs were synthesized using a similar procedure as described above. Typically for the growth of the $NaYF_4$ layer, 3 mL of OA, 7 mL of ODE, and 2 mL of $Y(CH_3CO_2)_3$ (0.2 M) stock solution were added into a 50-mL round bottom flask. The resulting mixture was heated to 150°C under stirring for 1 h. After cooling down to room temperature, the obtained $NaYF_4:20\%Yb^{3+},2\%Er^{3+}$ core NCs in the previous step were injected into the solution, and then, the mixed solution of 1 mL of NaOH-methanol (1 M) stock solution and 4 mL of NH_4F-methanol (0.4 M) stock solution was quickly added. Subsequently, the mixture was heated to 50°C, kept for 0.5 h, and then kept at 100°C for 1 h under vacuum to remove methanol. Finally, the mixture was heated to 290°C and incubated at 290°C for 1.5 h under an argon atmosphere. The resulting NCs were collected by centrifugation, washed with ethanol and cyclohexane, and dispersed in cyclohexane for subsequent use.

4.4 Fabrication of Silica FMS

The silica FMSs were fabricated using the surface tension of melted glass.[30] First, the commercial single-mode silica fiber ($SMF-28e^+$, Corning Incorporated, Corning, New York, United States) was stripped off the organic coating layer and cleaned with ethanol. Then, the cleaned fiber was suspended on a 3D adjustable stage and heated by a focused CO_2 laser beam within a narrow region. Due to the surface tension, a tapered fiber region was produced under a moderated laser power. The waist diameter of the tapered fiber can be controlled by adjusting the laser power and the distance between the silica fiber and the CO_2 laser focus. Subsequently, the obtained tapered fiber was cut into a half-taper. After remelting using the focused CO_2 laser beam, a microsphere cavity was created by the surface tension of melted glass. Notably, the microsphere cavity size can be finely controlled by slowly moving the tapered fiber along the half-taper.

4.5 Characterizations

The surface morphology of FMSs and NC@FMSs was observed by a field emission-SEM (Nova NanoSEM430, FEI, Eindhoven, Netherlands) with an accelerating voltage of 10 kV. The structure information of the as-synthesized core and core-shell NCs was analyzed using an X-ray diffractometer (D8 Advanced, Bruker Corporation, Karlsruhe, Germany) with Cu-Kα radiation. The morphology and microstructure of the as-synthesized core and core-shell NCs were acquired through transmission electron microscopy (JEM-2100F, JEOL, Tokyo, Japan). The microscopic photographs and microscopic fluorescent photographs of NC@FMSs were taken using a microscopic imaging system (Zolix Corp, Beijing, China). The UC emission signals of NC@FMSs were captured using a fiber optic spectrometer (QE65000, Ocean Optics, Dunedin, Florida, United States) with a 980 nm fiber laser as the excitation source. The UC emission signals of monodisperse core and core-shell NCs were captured through an iHR 320 spectrometer (Jobin-Yvon, Paris, France), and the excitation source was a 980 nm laser diode (LEO Photoelectric Technology, Guangzhou, China). The organic groups in $NaYF_4:20\%Yb^{3+},2\%Er^{3+}@NaYF_4$ core-shell NCs were detected by Fourier-transform infrared spectroscopy (Vertex-33, Bruker, Karlsruhe, Germany).

4.6 Theoretical Background of Temperature Sensing Based on Emissions from Er^{3+}

The luminescence intensity of an emission band can be expressed as[41]

$$I_{ij} = h\nu_{ij}A_{ij}N_i, \tag{1}$$

where h is the Planck constant, ν_{ij} is the transition frequency per photon from an i level to a j level; so $h\nu_{ij}$ is the transition energy per photon from an i level to a j level. A_{ij} and N_i are the spontaneous radiative emission probability and the level population in i level, respectively. In a thermometer based on the FIR technique, FIR defined using the emission intensities of the $E_2 \rightarrow E_0(I_2)$ and $E_1 \rightarrow E_0(I_1)$ transitions can be given by

$$\mathrm{FIR} = \frac{I_2}{I_1} = \frac{h\nu_{20}A_{20}N_2}{h\nu_{10}A_{10}N_1}, \tag{2}$$

where E_0 denotes the ground level, while E_2 and E_1 are the excited levels (level E_2 is more energetic than level E_1). If the two excited levels E_2 and E_1 are in thermal equilibrium, they are called "TCLs" and have energetic separations of the order of the thermal energy k_BT. N_2 and N_1 are related by,[3]

$$N_2 = \frac{g_2}{g_1} N_1 \exp\left(-\frac{\Delta E}{k_B T}\right), \tag{3}$$

where g_2 and g_1 are the degeneracies of the two corresponding levels, k_B is the Boltzmann constant, and ΔE is the energy gap between the E_2 and E_1 levels. Thus, Eq. (2) can be written as

$$\mathrm{FIR} = \frac{g_2 h\nu_{20} A_{20}}{g_1 h\nu_{10} A_{10}} \exp\left(-\frac{\Delta E}{k_B T}\right) = B \exp\left(-\frac{\Delta E}{k_B T}\right), \tag{4}$$

in which $B = \frac{g_2 h\nu_{20} A_{20}}{g_1 h\nu_{10} A_{10}}$. The two excited levels E_2 and E_1 must not be separated too much in energy so that its thermalization can be neglected. Typically, ΔE ranging from 200 to 2000 cm^{-1} is considered "thermally coupled" (e.g., in a thermodynamically quasi-equilibrium state).[42]

For Er^{3+}, the ${}^2\mathrm{H}_{11/2}$ and ${}^4\mathrm{S}_{3/2}$ levels belong to TCLs that can be thermally populated and depopulated with environmental temperature changes. The ${}^4\mathrm{S}_{3/2} \rightarrow {}^4\mathrm{I}_{15/2}$ and ${}^2\mathrm{H}_{11/2} \rightarrow {}^4\mathrm{I}_{15/2}$ transitions are in close proximity, which leads to a thermal equilibrium governed by the Boltzmann factor. Accordingly, Er^{3+}-doped NCs in this work can be used for accurate temperature measurement through the FIR technique using the temperature-dependent green emissions from the ${}^2\mathrm{H}_{11/2} \rightarrow {}^4\mathrm{I}_{15/2}$ and ${}^4\mathrm{S}_{3/2} \rightarrow {}^4\mathrm{I}_{15/2}$ transitions.

When the temperature is determined based on the knowledge of thermodynamic laws and quantities, the thermometer is termed primary.[3] Balabhadra et al.[43] proved that ΔE and B can be measured independently of any experimental calibration procedure, revealing that the temperature is only determined by the thermodynamic laws and quantities when using the FIR technique. Hence, the FIR thermometers based on the TCLs are the intrinsically luminescent primary thermometers. This is a significant step forward because Eq. (4) can be used to predict the temperature calibration curve. Namely, a function relation between the FIR and the temperature can be determined through fitting data points recorded at different temperatures according to Eq. (4). Then, the obtained relation ensures our designed NC@FMS all-fiber temperature sensor to be used as a precise thermometer in various fields.

Thermal sensitivity is a key parameter to evaluate the temperature measurement performance of a thermometer, defined as the rate of change of the thermometric parameter in response to the variation of temperature. The absolute sensitivity (S_a) is expressed as[44]

$$S_\mathrm{a} = \frac{\mathrm{d(FIR)}}{\mathrm{d}T} = \mathrm{FIR}\frac{\Delta E}{k_B T^2}. \tag{5}$$

Therefore, the S_a depends only on the scale of the thermally induced changes in FIR. It is meaningless to quantitatively compare the S_a among different Er^{3+}-doped materials. To compare the performance of distinct Er^{3+}-doped thermometers, irrespective of the host matrix, the relative sensitivity (S_r) should be adopted,

$$S_\mathrm{r} = \frac{1}{\mathrm{FIR}}\frac{\mathrm{d(FIR)}}{\mathrm{d}T} = \frac{\Delta E}{k_B T^2}. \tag{6}$$

S_r is usually expressed in units of percent change per degree of temperature change ($\%\ \mathrm{K}^{-1}$).

Code and Data Availability

Data underlying the results presented in this paper may be obtained from the corresponding authors upon reasonable request. All software is also available from the corresponding authors upon reasonable request.

Acknowledgments

This work was supported by the National Natural Science Foundation of China (Grant Nos. 52202004, 62122027, 12204179, 62205109, and 62075063), the Key R&D Program of Guangzhou (Grant No. 202007020003), the fellowship of China Postdoctoral Science Foundation (Grant Nos. 2021M691054 and 2022M711185), the Guangdong Basic and Applied Basic Research Foundation (Grant Nos. 2021A1515110475, 2021A1515110911, 2022A1515011289, and 2023A1515012666), the Guangzhou Basic and Applied Basic Research Foundation (Grant Nos. 202201010428 and 202201010407), the Local Innovative and Research Teams Project of Guangdong Pearl River Talents Program (Grant No. 2017BT01X137), and the State Key Lab of Luminescent Materials and Devices, South China University of Technology. We acknowledge H. Liang for helping in the preparation of the NCs.

References

1. J. J. Zhou et al., "Advances and challenges for fluorescence nanothermometry," *Nat. Methods* **17**, 967–980 (2020).
2. C. D. S. Brites et al., "Instantaneous ballistic velocity of suspended Brownian nanocrystals measured by upconversion nanothermometry," *Nat. Nanotechnol.* **11**, 851–856 (2016).
3. C. D. S. Brites, S. Balabhadra, and L. D. Carlos, "Lanthanide-based thermometers: at the cutting-edge of luminescence thermometry," *Adv. Opt. Mater.* **7**, 1801239 (2019).
4. H. Suo et al., "Rational design of ratiometric luminescence thermometry based on thermally coupled levels for bioapplications," *Laser Photonics Rev.* **15**, 2000319 (2021).
5. J. S. Donner et al., "Mapping intracellular temperature using green fluorescent protein," *Nano Lett.* **12**, 2107–2111 (2012).
6. K. Okabe et al., "Intracellular temperature mapping with a fluorescent polymeric thermometer and fluorescence lifetime imaging microscopy," *Nat. Commun.* **3**, 1714 (2012).
7. P. Low et al., "High-spatial-resolution surface-temperature mapping using fluorescent thermometry," *Small* **4**, 908–914 (2008).
8. F. Vetrone et al., "Temperature sensing using fluorescent nanothermometers," *ACS Nano* **4**, 3254–3258 (2010).
9. S. Kalytchuk et al., "Temperature-dependent exciton and trap-related photoluminescence of CdTe quantum dots embedded in a NaCl matrix: implication in thermometry," *Small* **12**, 466–476 (2016).
10. Z. H. Zhou et al., "Nonlinear thermal emission and visible thermometry," *Adv. Photonics* **4**, 045001 (2022).
11. R. G. Geitenbeek et al., "In situ luminescence thermometry to locally measure temperature gradients during catalytic reactions," *ACS Catal.* **8**, 2397–2401 (2018).
12. C. Mi et al., "Ultrasensitive ratiometric nanothermometer with large dynamic range and photostability," *Chem. Mater.* **31**, 9480–9487 (2019).
13. G. Kucsko et al., "Nanometre-scale thermometry in a living cell," *Nature* **500**, 54–58 (2013).
14. M. Xu et al., "Ratiometric nanothermometer in vivo based on triplet sensitized upconversion," *Nat. Commun.* **9**, 2698 (2018).
15. L. N. He, S. K. Ozdemir, and L. Yang, "Whispering gallery microcavity lasers," *Laser Photonics Rev.* **7**, 60–82 (2013).

16. B. Jiang et al., "Simultaneous ultraviolet, visible, and near-infrared continuous-wave lasing in a rare-earth-doped microcavity," *Adv. Photonics* **4**, 046003 (2022).
17. X. Jiang et al., "Whispering-gallery sensors," *Matter* **3**, 371–392 (2020).
18. A. Fernandez-Bravo et al., "Continuous-wave upconverting nanoparticle microlasers," *Nat. Nanotechnol.* **13**, 572–577 (2018).
19. Y. F. Shang et al. "Low threshold lasing emissions from a single upconversion nanocrystal," *Nat. Commun.* **11**, 6156 (2020).
20. S. L. Kang et al., "Enhanced 2 μm mid-infrared laser output from Tm^{3+}-activated glass ceramic microcavities," *Laser Photonics Rev.* **14**, 1900396 (2020).
21. X. Yang et al., "Fiber optofluidic microlasers: structures, characteristics, and applications," *Laser Photonics Rev.* **16**, 2100171 (2022).
22. Y. F. Xiong and F. Xu, "Multifunctional integration on optical fiber tips: challenges and opportunities," *Adv. Photonics* **2**, 064001 (2020).
23. W. Yan et al., "Thermally drawn advanced functional fibers: new frontier of flexible electronics," *Mater. Today* **35**, 168–194 (2020).
24. G. M. Tao et al., "Infrared fibers," *Adv. Opt. Photonics* **7**, 379–458 (2015).
25. G. M. Tao et al., "Multimaterial fibers," *Int. J. Appl. Glasss Sci.* **3**, 349–368 (2012).
26. M. Ferrera et al., "Low-power continuous-wave nonlinear optics in doped silica glass integrated waveguide structures," *Nat. Photonics* **2**, 737–740 (2018).
27. Q. W. Pan et al., "Nanocrystal-in-glass composite (NGC): a powerful pathway from nanocrystals to advanced optical materials," *Prog. Mater. Sci.* **130**, 100998 (2022).
28. L. Yang and K. J. Vahala, "Gain functionalization of silica microresonators," *Opt. Lett.* **28**, 592–594 (2003).
29. H. Takashima et al., "Fiber-microsphere laser with a submicrometer sol-gel silica glass layer codoped with erbium, aluminum, and phosphorus," *Appl. Phys. Lett.* **90**, 101130 (2007).
30. P. T. Snee et al., "Whispering-gallery-mode lasing from a semiconductor nanocrystal/microsphere resonator composite," *Adv. Mater.* **17**, 1131–1136 (2005).
31. T. C. Ouyang et al., "Microlaser output from rare-earth ion-doped nanocrystal-in-glass microcavities," *Adv. Opt. Mater.* **7**, 1900197 (2019).
32. B. Zhou et al., "NIR II-responsive photon upconversion through energy migration in an ytterbium sublattice," *Nat. Photonics* **14**, 760–766 (2020).
33. H. Fares et al., "Nano-silver enhanced luminescence of Er^{3+} ions embedded in tellurite glass, vitro-ceramic and ceramic: impact of heat treatment," *RSC Adv.* **6**, 31136–31145 (2016).
34. N. Bogdan et al., "Synthesis of ligand-free colloidally stable water dispersible brightly luminescent lanthanide-doped upconverting nanoparticles," *Nano Lett.* **11**, 835–840 (2011).
35. R. T. Wu et al., "Optical depletion mechanism of upconverting luminescence and its potential for multi-photon STED-like microscopy," *Opt. Express* **23**, 32401–32412 (2015).
36. X. Y. Li et al., "Two-wavelength two-photon process for optical selection of rare-earth ions," *J. Alloy. Compd.* **660**, 226–230 (2016).
37. D. J. Gargas et al., "Engineering bright sub-10-nm upconverting nanocrystals for single-molecule imaging," *Nat. Nanotechnol.* **9**, 300–305 (2014).
38. L. Yan et al., "Activating ultrahigh thermoresponsive upconversion in an erbium sublattice for nanothermometry and information security," *Nano Lett.* **22**, 7042–7048 (2022).
39. D. D. Yang et al., "Weakening thermal quenching to enhance luminescence of Er^{3+} doped β-$NaYF_4$ nanocrystals via acid-treatment," *J. Am. Ceram. Soc.* **102**, 6027–6037 (2019).
40. T. Q. Trung et al., "A stretchable strain-insensitive temperature sensor based onfree-standing elastomeric composite fibers for on-body monitoring of skin temperature," *ACS Appl. Mater. Interfaces* **11**, 2317–2327 (2018).
41. S. A. Wade, S. F. Collins, and G. W Baxter, "Fluorescence intensity ratio technique for optical fiber point temperature sensing," *J. Appl. Phys.* **94**, 4743–4756 (2003).
42. A. H. Khalid and K. Kontis, "2D surface thermal imaging using rise-time analysis from laser-induced luminescence phosphor thermometry," *Meas. Sci. Technol.* **20**, 025305 (2009).
43. S. Balabhadra et al., "Upconverting nanoparticles working as primary thermometers in different media," *J. Phys. Chem. C* **121**, 13962–13968 (2017).
44. S. F. Collins et al., "Comparison of fluorescence-based temperature sensor schemes: theoretical analysis and experimental validation," *J. Appl. Phys.* **84**, 4649–4654 (1998).
45. J. J. Zhou et al., "Activation of the surface dark-layer to enhance upconversion in a thermal field," *Nat. Photonics* **12**, 154–158 (2018).
46. H. Suo et al., "Constructing multiform morphologies of $YF_3:Er^{3+}/Yb^{3+}$ up-conversion nano/micro-crystals towards sub-tissue thermometry," *Chem. Eng. J.* **313**, 65–73 (2017).
47. B. S. Cao et al., "Wide-range and highly-sensitive optical thermometers based on the temperature-dependent energy transfer from Er to Nd in Er/Yb/Nd codoped $NaYF_4$ upconversion nanocrystals," *Chem. Eng. J.* **385**, 123906 (2020).
48. P. Du et al., "Simultaneous phase and size manipulation in $NaYF_4:Er^{3+}/Yb^{3+}$ upconverting nanoparticles for a non-invasion optical thermometer," *New J. Chem.* **41**, 13855–13861 (2017).
49. H. Suo et al., "Sensitivity modulation of upconverting thermometry through engineering phonon energy of a matrix," *ACS Appl. Mater. Interfaces* **8**, 30312–30319 (2016).
50. M. H. Liu et al., "Multifunctional $CaSc_2O_4:Yb^{3+}/Er^{3+}$ one-dimensional nanofibers: electrospinning synthesis and concentration-modulated upconversion luminescent properties," *J. Mater. Chem. C* **5**, 4025–4033 (2017).
51. T. V. Gavrilovic et al., "Multifunctional Eu^{3+}-and Er^{3+}/Yb^{3+}-doped $GdVO_4$ nanoparticles synthesized by reverse micelle method," *Sci. Rep.* **4**, 4209 (2014).
52. M. Lin et al., "Facile synthesis of mono-disperse sub-20 nm $NaY(WO_4)_2:Er^{3+}, Yb^{3+}$ upconversion nanoparticles: a new choice for nanothermometry," *J. Mater. Chem. C* **7**, 2971–2977 (2019).
53. P. Du and J. S. Yu, "Near-infrared light-triggered visible upconversion emissions in Er^{3+}/Yb^{3+}-codoped $Y_2Mo_4O_{15}$ microparticles for simultaneous noncontact optical thermometry and solid-state lighting," *Ind. Eng. Chem. Res.* **57**, 13077–13086 (2018).

Dandan Yang received her BS (2014), MS (2017), and PhD (2020) degrees at the School of Materials Science and Engineering from the South China University of Technology (SCUT) under the supervision of Prof. Guoping Dong and Prof. Jianrong Qiu. She is now a postdoctoral fellow in the State Key Laboratory of Luminescent Materials and Devices at SCUT. Her research interest focuses on the design, preparation, and optical performance investigation of micro/nanoparticles.

Guoping Dong received his MS (2007) and PhD (2010) degrees from the Wuhan University of Technology and Shanghai Institute of Optics and Fine Mechanics, Chinese Academy of Sciences, respectively. Then, he was a research assistant (2010) and an associate professor (2011) at the South China University of Technology (SCUT). He is currently a full professor (2014) in the State Key Laboratory of Luminescent Materials and Devices at SCUT. His research focuses on the design, preparation, and optoelectronic properties of optical functional materials and devices.

Biographies of the other authors are not available.